Research Article | Vol. 24, No. 14 | 11 Jul 2016 | OPTICS EXPRESS 15456

Optics EXPRESS

Deconvolution approach for 3D scanning microscopy with helical phase engineering

CLEMENS ROIDER,[1] RAINER HEINTZMANN,[2,3] RAFAEL PIESTUN,[4] AND ALEXANDER JESACHER[1,*]

[1]*Division of Biomedical Physics, Innsbruck Medical University, Müllerstraße 44, 6020 Innsbruck, Austria*
[2]*Institute of Physical Chemistry and Abbe Center of Photonics, Friedrich-Schiller-University Jena, Helmholtzweg 4, Jena D-07743, Germany*
[3]*Leibniz Institute of Photonic Technology, Albert-Einstein-Strasse 9, Jena D-07745, Germany*
[4]*Department of Electrical and Computer Engineering, University of Colorado, Boulder, CO 80309, USA*
[*]*alexander.jesacher@i-med.ac.at*

Abstract: RESCH (REfocusing after SCanning using Helical phase engineering) microscopy is a scanning technique using engineered point spread functions which provides volumetric information. We present a strategy for processing the collected raw data with a multi-view maximum likelihood deconvolution algorithm, which inherently comprises the resolution gain of Pixel-Reassignment Microscopy. The method, which we term MD-RESCH (for multi-view deconvolved RESCH), achieves in our current implementation a 20% resolution advantage along all three axes compared to RESCH and confocal microscopy. Along the axial direction, the resolution is comparable to that of Image Scanning Microscopy. However, because the method inherently reconstructs a volume from a single 2D scan, a significantly higher optical sectioning becomes directly visible to the user, which would otherwise require collecting multiple 2D scans taken at a series of axial positions. Further, we introduce the use of a single-helical detection PSF to obtain an increased post-acquisition refocusing range. We present data from numerical simulations as well as experiments to confirm the validity of our approach.

OCIS codes: (110.6880) Three-dimensional image acquisition; (180.5810) Scanning microscopy; (100.1830) Deconvolution; (110.4850) Optical transfer functions;

References and links

1. A. Jesacher, M. Ritsch-Marte, and R. Piestun, "Three-dimensional information from two-dimensional scans: a scanning microscope with postacquisition refocusing capability," Optica **2**(3), 210–213 (2015).
2. T. Wilson, *Confocal Microscopy* (Academic: London, 1990).
3. C. J. R. Sheppard, "Super-resolution in Confocal Imaging," Optik **80**(2), 53–54 (1988).
4. C. Müller and J. Enderlein, "Image scanning microscopy," Phys. Rev. Lett. **104**(19), 198101 (2010).
5. S. Quirin and R. Piestun, "3-D Imaging Using Helical Point Spread Functions," in Imaging Systems, OSA technical Digest (CD) (Optical Society of America, 2010), paper IWC1.
6. R. Piestun and S. Quirin, "Methods and systems for three dimensional optical imaging, sensing, particle localization and manipulation," U.S. Patent No. 8,620,065. 31 Dec. 2013.
7. M. D. Lew, S. F. Lee, M. Badieirostami, and W. E. Moerner, "Corkscrew point spread function for far-field three-dimensional nanoscale localization of pointlike objects," Opt. Lett **36**(2), 202–204 (2011).
8. M. Bertero, C. De Mol, E. R. Pike, and J. G. Walker, "Resolution in Diffraction-limited Imaging, a Singular Value Analysis," Optica Acta: International Journal of Optics **31**(8), 923–946 (1984).
9. M. Bertero, P. Brianzi, and E. R. Pike, "Super-resolution in confocal scanning microscopy," Inverse Problems **3**(2), 195–212 (1987).
10. S. Roth, C. J. R. Sheppard, K. Wicker, and R. Heintzmann, "Optical Photon Reassignment Microscopy," http://arxiv.org/abs/1306.6230, (2010).
11. A. G. York, P. Chandris, D. Dalle Nogare, J. Head, P. Wawrzusin, R. S. Fischer, A. Chitnis, and H. Shroff, "Instant super-resolution imaging in live cells and embryos via analog image processing," Nat. Meth. **10**(11), 1122–1126 (2013).
12. G. M. R. De Luca, R. M. P. Breedijk, R. A. J. Brandt, C. H. C. Zeelenberg, B. E. de Jong, W. Timmermans, L. N. Azar, R. A. Hoebe, S. Stallinga, and E. M. M. Manders, "Re-scan confocal microscopy: scanning twice for better resolution," Biomed. Opt. Express **4**(11), 2644–2656 (2013).

#262534 http://dx.doi.org/10.1364/OE.24.015456
Journal © 2016 Received 6 Apr 2016; revised 5 Jun 2016; accepted 5 Jun 2016; published 29 Jun 2016

Optics EXPRESS

13. R. Heintzmann, G. Kreth, and C. Cremer, "Reconstruction of Axial Tomographic High Resolution Data from Confocal Fluorescence Microscopy: A Method for Improving 3D FISH Images," Anal. Cell. Path. **20**(1), 7–15 (2000).
14. R. Heintzmann, Q. S. Hanley, D. Arndt-Jovin, and T. M. Jovin, "A dual path programmable array microscope (PAM): simultaneous acquisition of conjugate and non-conjugate images," J. of Microscopy, **204**(2), 119–135 (2001).
15. R. Heintzmann, V. Sarafis, P. Munroe, J. Nailon, Q. S. Hanley, and T. M. Jovin, "Resolution enhancement by subtraction of confocal signals taken at different pinhole sizes," Micron. **34**(6), 293–300 (2003).
16. M. Ingaramo, A. G. York, E. Hoogendoorn, M. Postma, H. Shroff, and G. G. Patterson, "Richardson-Lucy deconvolution as a general tool for combining images with complementary strengths," Chem. Phys. Chem. **15**(4), 794–800 (2014).
17. R. Piestun, B. Spektor, and J. Shamir, "Unconventional light distributions in three-dimensional domains," J. of modern optics **43**(7), 1495–1507 (1996).
18. R. Piestun and J. Shamir, "Control of wave-front propagation with diffractive elements," Opt. Lett. **19**(11), 771–773 (1994).
19. R. Piestun, Y. Y. Schechner, and J. J. Shamir, "Propagation-invariant wave fields with finite energy," Opt. Soc. Am. A. **17**(2), 294–303 (2000).
20. W. H. Richardson, "Bayesian-Based Iterative Method of Image Restoration," J. Opt. Soc. Am. **62**(1), 55–59 (1972).
21. J.-B. Sibarita, "Deconvolution Microscopy," in *Microscopy Techniques*, (Springer Berlin Heidelberg 2005).
22. D. S. C. Biggs and M. Andrews, "Acceleration of iterative image restoration algorithms," Appl. Opt. **36**(8), 1766–1775 (1997).
23. M. Gu, *Advanced optical imaging theory* (Springer Science & Business Media, 1999).
24. R. Heintzmann, "Estimating missing information by maximum likelihood deconvolution," Micron. **38**(2), 136–144 (2007).

1. Introduction

RESCH microscopy [1] is a scanning microscopy with detector array collection and helical pupil phase engineering in the detection path. When implemented with a double helix, the image of a fluorescent point scanned by the excitation focus appears as a double-lobe on the detector whose orientation contains information about the emitter's axial location. Exploiting this principle, we have recently demonstrated that RESCH allows sectioning and volume reconstruction of the sample after the acquisition has been performed, within an axial range that is mainly defined by the length of the excitation focus. Extracting a slice off the nominal focal plane is achieved by applying appropriate synthetic pinhole (SP) pairs to the raw images acquired at every single sampling point. While the axial position of the confocal image obtained this way depends on the rotational angle of the chosen pinhole-pair, its spatial resolution depends on the pinhole size, just like in a standard confocal microscope [2]. The highest achievable resolution corresponds to a pinhole-pair consisting of merely two individual pixels (one per pinhole). The implied low light throughput however demands choosing larger pinholes for most applications, thereby trading resolution against signal.

Here we present a method to process the raw data collected by a RESCH microscope, which improves the spatial resolution of RESCH microscopy as presented in [1]. Our approach, which we name MD-RESCH (for "multi-view deconvolved" RESCH) is purely numerical (after the fact that images are obtained with engineered point spread functions (PSFs)) and can be understood as a generalization of the principle used in Image Scanning Microscopy [3, 4]. Therefore it is also applicable to any other camera-based scanning microscope, regardless of the shape of the PSF used.

Furthermore, we prove the feasibility of a single helix detection PSF [5–7]. In contrast to widefield localization microscopies, the single-helix can retrieve depth from a single recording in RESCH, because there is no ambiguity between lateral position and rotation. The single-helix variant used for this work offers better refocusing performance than the double-helix used in [1] and has the additional advantage of a more compact shape (one lobe instead of two) and thus a better signal to noise ratio.

Optics EXPRESS

This paper is organized as follows: In section 2, we briefly review the principle of Image Scanning Microscopy and compare it to RESCH using engineered and non-Gaussian PSFs. In section 3 we provide details to our single-helix detection PSF design. Section 4 explains our multi-view deconvolution approach. Numerical and experimental investigations on the obtainable spatial resolution are presented in section 5, followed by a simulated imaging example (section 6) and experimental results from stained microtubules in COS-7 cells (section 7).

2. Spatial resolution in confocal microscopy using pixelated detectors

Resolution improvement in confocal scanning microscopy using pixelated detection was investigated in the 1980's [3,8,9]. A simple and effective pathway to process the camera data in such a configuration was provided in 1988 by Colin Sheppard [3]. Probably due to the lack of suitable detectors at the time, however, the experimental realization of the principle occurred more than 20 years later [4], under the name *Image Scanning Microscopy* (ISM). We briefly review the principle of ISM in the following.

The PSF of an incoherent confocal imaging system with a point-like pinhole located on the optical axis is the product of the excitation and detection PSFs, i.e. $h(x) = h_{ex}(x) \cdot h_{det}(x)$ [2]. This PSF is further referred to as "combined PSF". When a camera is used as detector, with proper magnification, each pixel can be essentially considered a point-like pinhole. Each of these "pixel-pinholes" delivers an individual single-detector confocal image at a resolution close to the theoretical maximum. One can now add up all single-detector confocal images in order to generate a high resolution confocal image with a significantly increased signal to noise ratio (SNR). Before adding up, however, one must compensate transverse shifts that exist between the images, which are a consequence of the different positions of the camera pixels. The influence of the pixel position on the image shift is depicted in Fig. 1. Here we assume a magnification of one for the sake of simplicity. If we assume stage-scanning, the excitation PSF remains on the optical axis, i.e. $h_{ex}(x) \propto G(x, \sigma_{ex})$, with $G(x,\sigma) = exp(-x^2/\sigma^2)$. Conversely, the detection PSF can be thought of being placed on the position in the sample plane which is conjugate to the pixel-pinhole: $h_{det}(x) \propto G(x - \hat{x}_m, \sigma_{det})$, where $\hat{x}_m$ is the distance of pixel m from the optical axis.

Optics EXPRESS

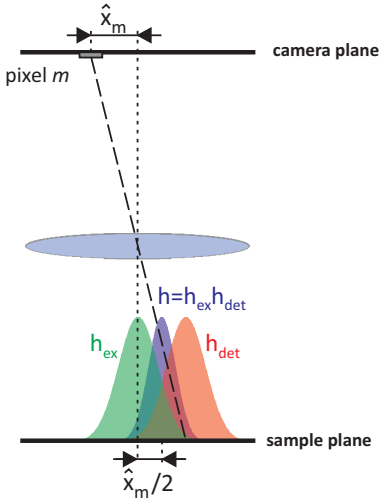

Fig. 1. Point spread function of a confocal microscope with a point-like off-axis detector: the combined PSF, which is the product of the excitation and detection PSFs, is shifted by half of the distance the detector has from the optical axis. This is however only valid for PSFs whose shapes fulfill certain symmetry conditions, such as e.g. Gaussian PSFs.

Generally, the product of h_{ex} with h_{det} leads to the following expression for the combined PSF:

$$h(x) \propto G\left(x - \frac{\sigma_{ex}^2}{\sigma_{ex}^2+\sigma_{det}^2}\hat{x}_m, \frac{\sigma_{ex}\sigma_{det}}{\sqrt{\sigma_{ex}^2+\sigma_{det}^2}}\right), \tag{1}$$

which simplifies to

$$h(x) \propto G\left(x - \frac{\hat{x}_m}{2}, \frac{\sigma_{ex}}{\sqrt{2}}\right) \tag{2}$$

if we neglect the Stokes shift. In this case the combined PSF is centered on the midpoint between optical axis and pixel position $\hat{x}_m$. This means that, prior to summation, each confocal image has to be shifted back by *half* of the distance between the pixel-pinhole and the optical axis. This translation can be done numerically, but also optically [10–12].

Obviously, the procedure outlined above is only valid for PSFs whose shapes fulfill certain symmetry conditions, such as for instance Gaussian PSFs. For arbitrary detection and/or excitation PSFs, the collected single-detector confocal images are blurred by combined PSFs which may have individual shapes and locations. Hence, in order to achieve improved resolution, the procedure of image *back-shifting* (also denoted as "pixel-reassignment") has to be replaced by the more general approach of deconvolution from multi-sensor data [13–16]. Such algorithms aim at estimating the most likely image of an object based on several different images taken with varying PSFs.

3. Design of a single-helix detection PSF

The generation of single-helical beams has first been reported by Piestun et al. in 1996 [17]. A general pathway for the engineering of helical PSFs exists in the employment of an algorithm, which iteratively projects light fields onto defined constraint sets [18], in conjunction with a suitable starting condition. Such a starting condition has been shown to exist in the superposition of selected Gauss-Laguerre modes [7, 19]. The phase profile of the mode superposition is a diffractive phase pattern that already produces a single-helix PSF. This pattern serves as starting

Optics EXPRESS

condition for the iterative algorithm, which improves on the PSF properties by successively propagating to multiple PSF cross sections, where intensity constraints replace the single-lobed intensity profiles by Gaussian fits. Finally, the light fields in all planes are back-propagated to the phase mask, where they are averaged to form the new field for the following iteration. Usually, the algorithm converges quickly, after some tens of iterations. In our particular case, we use Gauss-Laguerre modes with the following radial (r) and azimuthal (a) indices to form the initial phase mask: (r,a)=(1, 1); (2, 4); (3, 7); (4, 10); (5, 13). The algorithm propagates to 11 planes, which are equally spread over a z-range of 4 µm. Figure 2 shows the phase mask (left) and an iso-intensity surface plot (NA 1.25, wavelength 660 nm) of the final single-helix PSF. The PSF's total angle of rotation is less than 360Âř, which is why ambiguities in assigning sample structures their correct depths cannot occur.

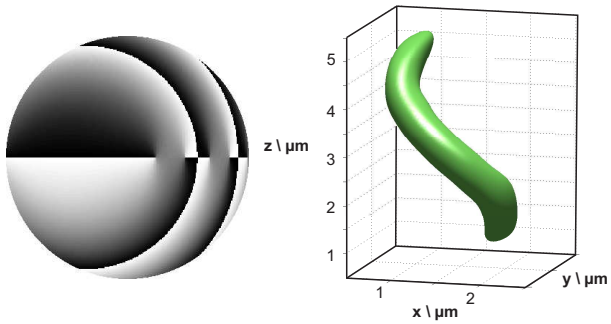

Fig. 2. Phase mask (left) to shape the detection PSF. Gray values correspond to phase values. An iso-intensity surface plot of the corresponding single-helix PSF is shown on the right (NA=1.25, wavelength=660 nm); length scales apply to a medium with refractive index of 1.52

.

4. Multi-view deconvolution in RESCH microscopy

RESCH [1] is a camera-based scanning technique in the sense that it collects an image (e.g. 20 $\times$ 20 pixels) around the focus location at every single scan point. The collected data can thus be expressed as a 4D dataset: $D(x,y,\hat{x}_m,\hat{y}_m)$, with x,y denoting the 2D scan position and $\hat{x}_m,\hat{y}_m$ the lateral coordinates of the detector pixel m. In the course of a scan, every camera pixel m detects its own confocal image $I_m(x,y)$ with an imaging performance defined by a 3D intensity PSF $h_m(x,y,z)$. If we approximate the shape of a pixel m by the delta function $\delta(x-\hat{x}_m,y-\hat{y}_m)$, these PSFs can be expressed as [1]

$$h_m(x,y,z) = [\delta(x-\hat{x}_m,y-\hat{y}_m) *_{2D} h_{det}(x,y,z)]\ h_{ex}(x,y,z). \tag{3}$$

Here, the symbol $*_{2D}$ represents the two-dimensional convolution operator acting in the x,y plane. The peculiarity of RESCH is that these $h_m(x,y,z)$ have substantially varying axial positions. Descriptively, this can be understood by considering that some camera pixels are only exposed to light if an observed light emitter is out of focus such that its helix-image appears sufficiently rotated to cover these pixels. It is important to note that the combined imaging PSFs h_m do *not* exhibit helical shapes such as h_{det}, but look quite similar to confocal PSFs [1].

We employ a maximum likelihood multi-view deconvolution algorithm based on the Richardson-Lucy (RL) algorithm [20, 21]. In an iterative fashion, the algorithm estimates a 3D object from the set of given 2D single-detector confocal images $I_m(x,y)$ and the corresponding

Optics EXPRESS

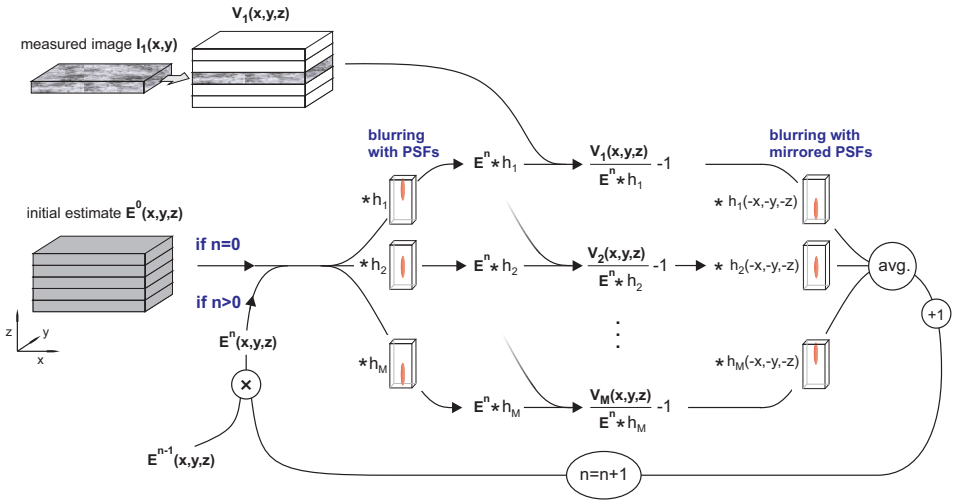

Fig. 3. Flow diagram of the multi-view Richardson-Lucy algorithm.

.

3D PSFs $h_m(x,y,z)$:

$$E^{n+1}(\mathbf{r}) = E^n(\mathbf{r}) \cdot \left\{ \frac{1}{M} \sum_{m=1}^{M} \left[\left(\frac{V_m(\mathbf{r})}{E^n(\mathbf{r}) * h_m(\mathbf{r})} - 1 \right) * h_m^*(-\mathbf{r}) \right] + 1 \right\}. \tag{4}$$

The equation above describes a basic implementation, which can be derived in analogy to the original RL algorithm [21] under consideration of taking multiple independent views. Here, $E(\mathbf{r})$ is the estimate of the object. The quantities V_m correspond to volume grids containing the measured confocal images $I_m(x,y)$ in their middle slices, and zeros elsewhere (see Fig. 3). M denotes the total number of detector pixels used, i.e., the number of different views. Prior to dividing by $E^n * h_m$ it is sensible to replace too small values in this expression by a user-defined threshold value, e.g. 10^{-8}, in order to avoid singularities in the ratios. The initial estimate E^0 is defined as a volume grid filled with a constant value corresponding to the average intensity over all measurements I_m. The variable $\mathbf{r}$ represents the 3D coordinate vector: $\mathbf{r} = (x,y,z)$. Note that $h_m^* \equiv h_m$ as the PSFs are real-valued. A flow diagram of the algorithm working principle is shown in Fig. 3. For our work we employed an accelerated version of this basic scheme in terms of convergence speed [22]. Based on simulations and comparing the deconvolved data with the ground truth, we find that the accelerated version obtains a similar RMS error after only half as many iterations, when compared to the performance of the basic scheme outlined in Eq. 4. This result was found for the "tree-example (3 views)" shown in Fig. 7. We would like to note, however, that the performance gain will generally depend on the problem at hand.

5. Spatial resolution and refocusing range

The spatial resolution and refocusing range of MD-RESCH are investigated by inspecting the dimensions of numerically calculated and experimentally measured PSFs h_m. The simulated PSFs are derived by first calculating the 3D excitation PSF using the vectorial Debye approximation [23], followed by simulating a 3D stage-scan over a single fluorescing sample point and calculating the single-helix response on the camera for every single scan step. The intensity variations at camera pixel m due to the 3D stage scanning define the PSF $h_m(x,y,z)$. The excitation polarization is assumed linear for RESCH and circular for ISM. The scan steps are 97 nm in the

Optics EXPRESS

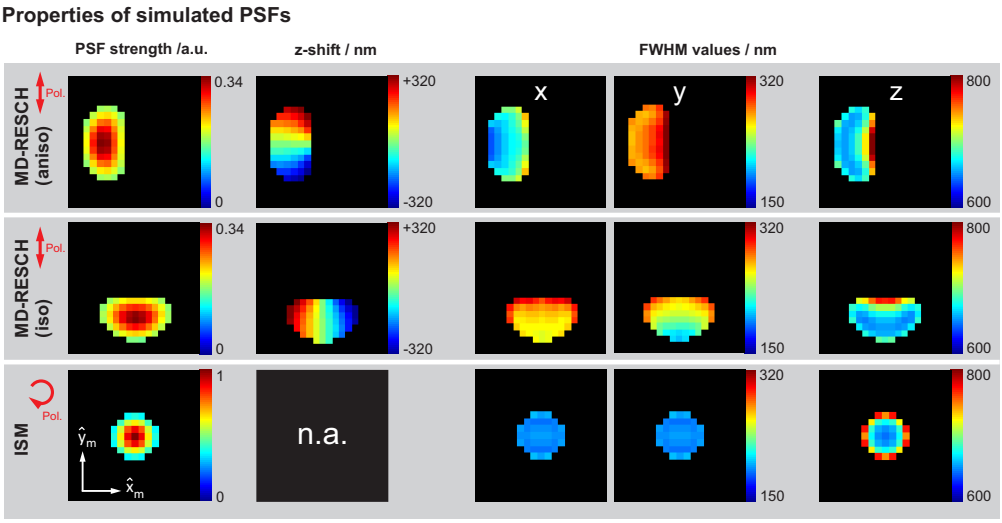

Fig. 4. Properties of **simulated** PSFs for every detector pixel (NA=1.25, wavelength: ex./em.= 640/660 nm). The properties are color-coded in the respective pixels. Compared are three methods: MD-RESCH for different helix orientations and ISM. The red arrows on the left indicate the excitation laser polarization. 1st column: Integrated PSF-strengths; 2nd column: axial PSF shifts, determined as z-centroid coordinates of 3D Gaussian fits to the simulated PSFs; 3rd-5th columns: FWHM-values of 3D Gaussian fits to the PSFs;

lateral directions and 100 nm in the axial direction. The numerical light propagation along the detection path likewise considers vectorial effects. Here we assume that the fluorophore emits unpolarized light, regardless of the excitation polarization, i.e. it was modeled as three orthogonal and mutually incoherent dipole emitters of equal strengths. The aplanatic factors applied to the electric fields in the objective pupil for excitation and emission are $1/\sqrt{\cos(\theta)}$ and 1, respectively, with θ defined as the polar angle measured from the optical axis.

Figure 4 summarizes the results. The figure contains several images, each representing the detector array. Each pixel in the images corresponds to an individual detector pixel m. Properties of the PSFs that belong to the individual detector pixels are encoded in the respective pixel colors. Three methods are compared: MD-RESCH for differently oriented helix-PSFs with respect to the laser polarization (here denoted as MD-RESCH "iso" and "aniso") and ISM. One can see from the lateral PSF widths (3rd and 4th image column) that the helix orientation matters: if its long lobe axis lies parallel to the excitation polarization, we see a notable difference between the x- and y-resolutions (hence the label "aniso"). The reason for this anisotropy is that both, the long axis of the detection PSF as well as the y-directed polarization contribute to a lower resolution along the y-axis. The effect is more emphasized for high imaging NAs. However, both anisotropies compensate each other to a large extend if the long lobe-axis lies orthogonal to the polarization. This leads to an almost isotropic transverse resolution for the given NA.

The first image column in Fig. 4 shows total "strengths" of the PSFs h_m, i.e., $\sum_{x,y,z} h_m(x,y,z)$. The data of too "weak" pixels are discarded to restrict the amount of data: for the cases shown here, a threshold was set such that all PSFs with peak values below 25% of the strongest PSF's peak value are discarded (15% for the ISM case: this leads to a total detector area of the size of an Airy disc).

The second image column shows the axial PSF shifts. They correspond to the z-centroid coordinates of 3D Gaussian fits to the individual PSFs. In this configuration, MD-RESCH allows post-acquisition refocusing by approximately $\pm$400 nm at an NA of 1.25, which roughly equals

Optics EXPRESS

the z-resolution as defined by Rayleigh. Conversely, ISM shows only in-plane information. The last three columns contain full-width-at-half-maximum values of 3D Gaussian fits to the PSFs, thus providing estimates of the obtainable 3D resolutions.

Reducing the number of views

Faster data readout and thus compatibility with high-speed galvo scanning can be obtained by reducing the number of detector pixels, i.e. the number of views. In this case, the relatively slow camera can be replaced by a fast segmented photo-detector. Of course, this comes at the cost of a reduced spatial resolution as the "pixel reassignment advantage" is lost. Figure 5 shows the case of "binning" the 61 detector pixels of Fig. 4 to merely three large "super-pixels", according to the z-centroids of their PSFs: the entire refocusing range is grouped into three equal intervals and each detector pixel assigned to one of the three "super-pixels" according to the interval which contains the z-centroid of its PSF. The large "super-pixels" could in practice be the ends of light collecting fibers. In our example, the areas of the corresponding SPs are 0.5, 0.8 and 0.5 Airy discs. The PSFs of the SPs are calculated as the arithmetic averages of all PSFs that belong to pixels within the respective SPs. As these PSFs show mutual shifts along x, y and z, their average is wider along all axes and the resolution accordingly reduced. Also the refocusing range is reduced from about $\pm$400 to $\pm$300 nm. A quantitative comparison of average PSF

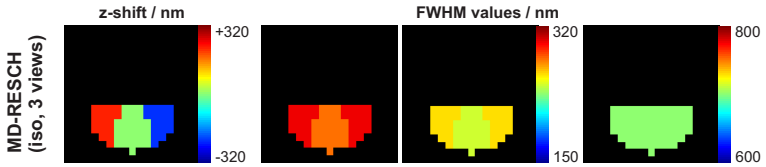

Fig. 5. Properties of **simulated** PSFs for three detectors for the MD-RESCH (iso) case. The properties are colour-coded in the respective detector areas. The helical RESCH PSFs are off-centered with respect to the optical axis. 1st column: axial PSF shifts; 2nd-4th columns: FWHM-values of 3D-Gaussian fits to the PSFs; refocusing range and PSF widths apply to a medium with refractive index of 1.52

Table 1. **Calculated** spatial resolution estimates (in nm) for MD-RESCH (iso and aniso, 61 views), MD-RESCH (iso, 3 views), ISM and confocal microscopy. The numbers are FWHM values of mean PSFs for the respective methods.

method	x	y	z
MD-RESCH (iso, 61 views)	250	230	650
MD-RESCH (aniso, 61 views)	210	280	660
MD-RESCH (iso, 3 views)	280	320	760
ISM	190	190	700
confocal	300	300	800

widths for MD-RESCH for 61 and 3 views, ISM and confocal microscopy (with Airy-disc-sized pinhole) is given in table 1. The numbers are rounded to 10 nm accuracy. The numbers show that the resolving power of MD-RESCH for 61 views surpasses that of the 3-view case by about 20% along all three axes and lies between that of a confocal microscope and ISM.

Measured PSFs

Figure 6 shows measured PSF properties for MD-RESCH (iso, 64 views) and ISM (38 views). Imaging parameters such as NA and wavelengths are the same as for the simulation. The thresholds to cut off "weak views" have been raised to 40% and 30% of the PSF peak value of the

Optics EXPRESS

strongest PSF such that the number of views becomes comparable to the simulations. We observe that all measured PSF widths are generally larger by about 20-30% compared to the simulations (see table 2). However, the relations between the PSF-widths for RESCH and ISM and the refocusing range are as predicted.

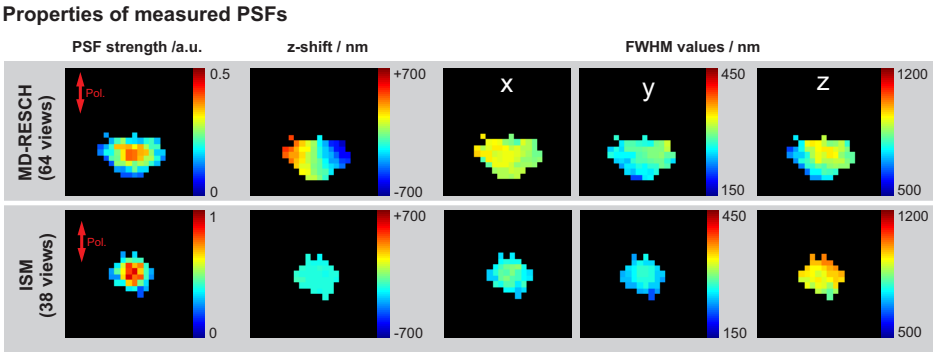

Fig. 6. **Measured** PSF properties for MD-RESCH (iso) and ISM.

.

Table 2. **Measured** FWHM values (in nm) of PSFs for MD-RESCH (iso, 64 views), MD-RESCH (iso, 3 views), ISM (38 views), and confocal microscopy (Airy-disc-sized pinhole).

method	x	y	z
MD-RESCH (iso, 64 views)	320	270	820
MD-RESCH (iso, 3 views)	380	340	1010
ISM	270	250	940
confocal	370	330	1110

.

6. Simulated imaging

We validate our approach by numerically simulating RESCH and MD-RESCH (iso) imaging of a fluorescent 3D sample (NA=1.25, ex./em. wavelengths=640/660 nm). Our assumed specimen is a sketch of an apple tree, which is designed as a 3D structure: leaves, branches and apples are located in three distinct axial planes, separated by 200 nm (see Fig. 7, "ground truth"). The size of the simulated scan area is 18×18 µm^2. A confocal image $I_m(x,y)$ is constructed for each pixel-pinhole m by numerically 3D-blurring the sample with h_m and taking the center-plane of the result, as this is the plane imaged onto the camera. Shot noise was assumed. The maximum number of photons at a single detector pixel was assumed to be about 70. This can be inferred from the top left image, which shows the confocal image of the "strongest" pixel-pinhole.

RESCH microscopy similar to as presented by Jesacher et al. [1] is simulated by adding up all single-pixel confocal images which belong to each of the three SPs defined for our 3-view-case (see Fig. 5). Differences to the original implementation [1] are that here, the SPs are not circularly shaped and that the emission PSF is a single-helix rather than a double-helix. These differences, however, have only a small influence on the image quality. The resulting three RESCH views are shown in the second image row. From these views, we obtain the 3-view MD-RESCH results by deblurring them with our accelerated multi-view deconvolution algorithm for 400 iterations using simulated PSFs. The results are shown in the third image row of Fig. 7. Finally, the last image row shows the results from simulated MD-RESCH imaging based on 61 views, which we likewise deblurred for 400 iterations using simulated PSFs. .

Optics EXPRESS

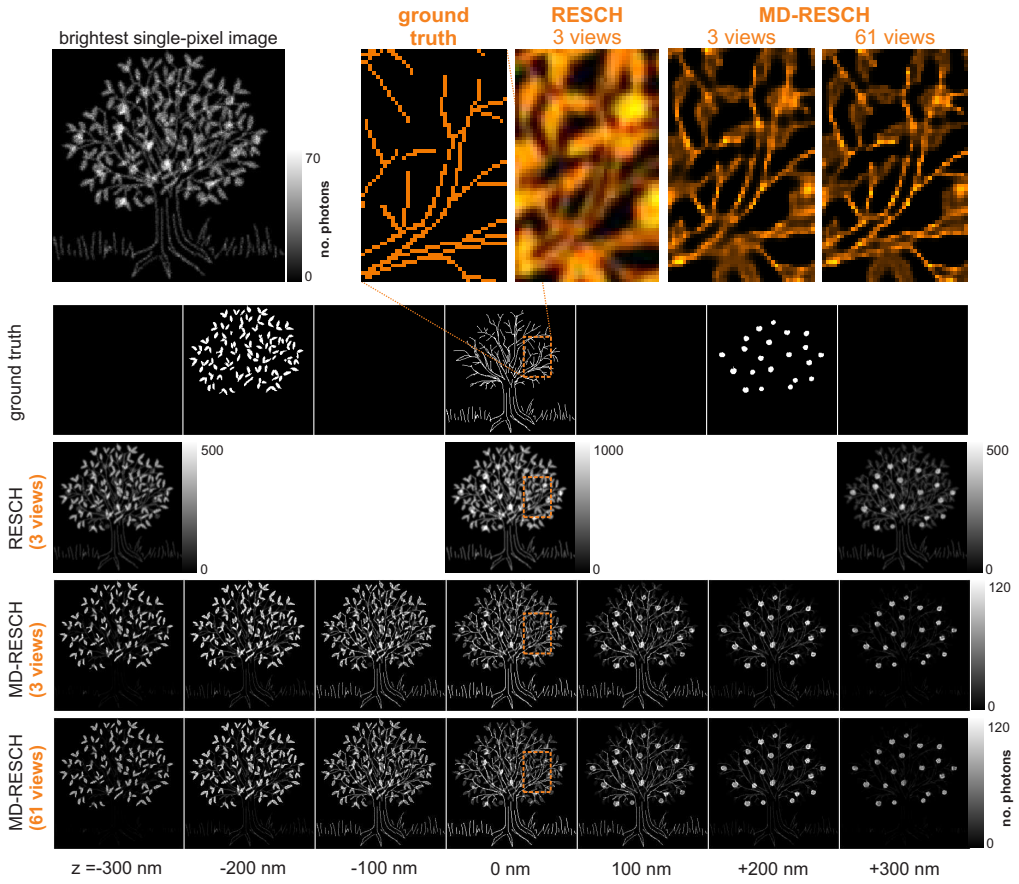

Fig. 7. Simulated MD-RESCH imaging: the assumed sample is a sketch of an apple tree with branches, leaves and apples in three different axial planes; top left image: confocal image of the strongest detector pixel; 1st image row: ground truth; 2nd row: RESCH based on the three SPs shown in Fig. 5; 3rd and 4th rows: MD-RESCH results (iso) for 3 and 61 detector pixels, after 400 deblurring iterations

Generally, the simulation proves that MD-RESCH is capable of imaging volumetric samples. The z-locations of apples, branches and leaves are reproduced in their correct depths. Comparing the three different methods reveals a clear 3D resolution advantage of the MD-RESCH methods over RESCH. This is little surprising considering that the RESCH images are not deconvolved at all. The “pixel-reassignment” effect, which discriminates the MD-RESCH 3-view from the 61-view case, leads to a further small resolution improvement. Differences between the corresponding tree reconstructions become visible at close inspection (see orange images). Comparing both deconvolution results with the ground truth, we find a 1% smaller RMS error for the 61-view case.

7. Experimental results

Figure 8 contains experimental MD-RESCH results from stained (Alexa 647) and fixed COS-7 cells on a cover slip. The imaging NA is 1.25. The experimental set-up is described in [1]. The only notable difference is the the type of detection PSF (here single-helix rather than double-helix). The image series in Fig. 8(a) shows different z-sections through a microtubule network.

Optics EXPRESS

All layers were generated from data collected in a single RESCH scan and subsequent deconvolution by 200 iterations based on 84 views (the larger number of views stems from choosing a lower threshold value for the PSFs h_m). Measured PSFs were used for the deconvolution. The larger image in the lower left corner exhibits an increased depth of focus. It is generated by computing the maximum intensity projection along z of the entire reconstructed sample volume (Visualization 1). The images in Fig. 8(b) highlight reconstruction differences that originate from taking different numbers of views. The 84-view result is better resolved than the 3-view result. Both reconstructions share the same raw data and were deconvolved for 50 iterations.

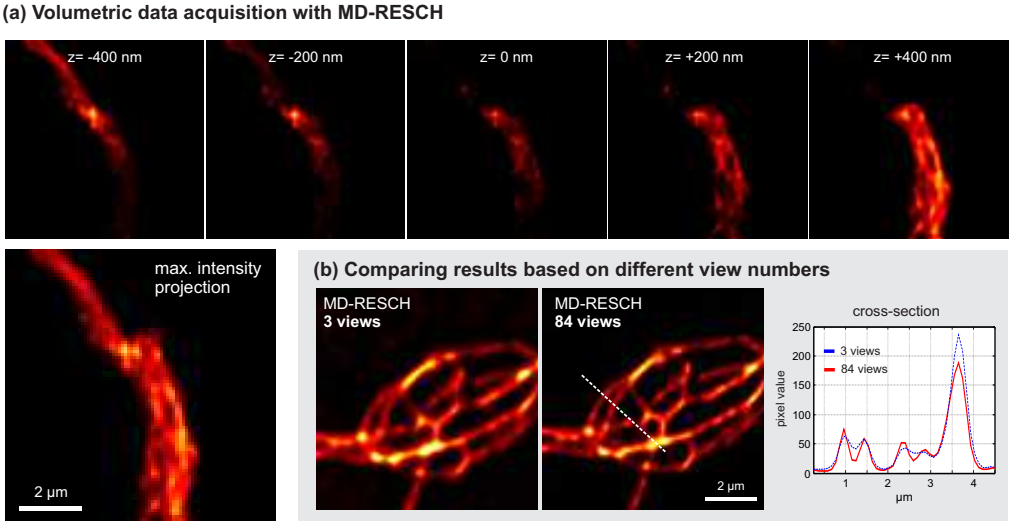

Fig. 8. a) MD-RESCH images from Alexa 647 stained microtubules in COS-7 cells (NA=1.25). The multi-view deconvolution comprised 200 iterations and is based on 84 views. Projecting the image volume along the optical axis generates a significantly increased depth of focus. The entire image volume is shown in (Visualization 1). b) Comparison of specimen reconstructions based on 3 and 84 views, respectively. Taking a larger number of views provides improved resolution, which is also shown by cross sections along the same region (marked by white dashed line) of both reconstructions.

8. Discussion and summary

We presented a multi-view 3D deconvolution approach for processing RESCH microscopy data. The approach, which we term MD-RESCH for "multi-view-deconvolved RESCH", represents a generalized version of pixel-reassignment and is as such applicable to scanning microscopy systems with arbitrary PSFs. The resolution advantage compared to RESCH as presented in [1] was found to be about 20% along all three axes. Thus, the resolution lies between that provided by ISM and confocal microscopy with Airy-disc-sized pinhole. We would like to emphasize that this resolution advantage is real in a sense that it is caused by an improved optical transfer function and not by numerical re-weighting of spectral components (such as e.g. done by Wiener deconvolution). However, the resolution gain of our deconvolution method appears to be significantly higher than 20%. We mainly ascribe this to the mentioned spectral re-weighting, although it is known that maximum likelihood deconvolution can also lead to a true increase of the frequency passband (see e.g. Ref. [24]). In this context, a remarkable feature of MD-RESCH is that it is capable of providing the "spectral re-weighting - induced" resolution gain even along the z-axis from a *single* 2D scan. Consequently, a single MD-RESCH image exhibits significantly higher optical sectioning than a single confocal image. Obtaining comparable

Optics EXPRESS

z-resolution from a confocal microscope requires taking multiple scans at different z-positions.

We introduced the use of a single-helix detection PSFs for RESCH, which provides a higher signal to noise ratio than the double-helix [1] as well as an approximately 20% larger refocusing range, which is comparable to the z-resolution. For MD-RESCH, it has the further advantage that a smaller number of pixels (views) have to be read out. We would like to emphasize that what we define as refocusing range is a rather soft-limited quantity. The numbers for "z-shifts" stated in this paper do only reflect the center-positions of PSFs and as such represent a lower limit. What can be achieved in practice depends on experimental parameters such as the signal to noise ratio and can easily exceed this nominal refocusing range. Preliminary simulations show that 3D reconstructions spanning even twice this range should be feasible. This is subject of ongoing investigations.

Acknowledgment

Our work is supported by the ERC Advanced Grant 247024 *catchIT* and the National Science Foundation (NSF) (1063407 and 1429782). This work was performed within the frame of the Christian Doppler Laboratory CDL-MS-MACH.